Nonlinear magnetization dynamics as a route to nonreciprocal phases, spin superfluidity, and analogue gravity

Vincent P. Flynn^{1,2} and Benedetta Flebus¹

¹Department of Physics, Boston College, Chestnut Hill, Massachusetts 02467, USA ²Department of Physics and Astronomy, Dartmouth College, Hanover, New Hampshire 03755, USA (Dated: October 28, 2025)

The identification of platforms with independently tunable nonlinearity and non-Hermiticity promises a quantitative route to far-from-equilibrium universality across many-body systems. Here we show that a conventional ferromagnetic multilayer realizes this paradigm: balancing a dc drive against Gilbert damping stabilizes a chiral spin-superfluid limit cycle that spontaneously breaks spacetime-translation symmetry. The resulting superflow is intrinsically nonreciprocal: long-wavelength magnons of opposite chirality acquire asymmetric dispersions and propagate direction-selectively, realizing a spin-superfluid diode. This asymmetry is flow-borne – it reflects broken Galilean invariance and requires neither structural asymmetry nor finely tuned gain-loss balance. Linearized dynamics in the comoving superfluid frame are intrinsically pseudo-Hermitian and, in the long-wavelength sector, can be mapped to a (1+1)D wave equation on curved spacetime. Spatial modulation of the drive enables the generation of sonic horizons that parametrically squeeze magnons and produce Hawking-like particle-hole emission. Our results establish a tabletop route from nonlinear dissipative-driven magnetization dynamics to nonreciprocal transport, nonequilibrium phase transitions, and analogue-gravity kinematics.

Introduction. — Most of the surrounding world operates far from equilibrium. In this regime, the interplay between energy non-conserving interactions and nonlinearities is an organizing principle that cuts across seemingly unrelated phenomena – from neural networks [1] to astrophysical flows [2] – where collective order is set by symmetries and conservation laws rather than microscopic detail, enabling sharp tests of universality.

Dissipative Rydberg arrays and exciton–polariton fluids have provided early platforms for quantitative tests that have established a paradigm for exploring universal behavior in open quantum systems [3–6]. The pace of theoretical advances, however, calls for platforms in which nonlinearity and non-Hermiticity can be easily tuned and precisely diagnosed with tabletop instrumentation. Such systems could enable parameter-resolved maps of dynamical phase diagrams and tests of universality, while opening access to properties unique to far-from-equilibrium physics such as critical behavior organized not by equilibrium free-energy landscapes, but by spectral singularities forbidden at thermal equilibrium [7–19].

With their intrinsic dissipative and nonlinear dynamics [20], and well-established protocols for spin injection, magnetic systems appear as promising, low-overhead solid-state candidates. Yet most explorations of their non-Hermitian properties have remained confined to the linear regime [21–30].

Here we move beyond this regime and demonstrate that the interplay of drive, dissipation, and coherent interactions in a conventional ferromagnetic heterostructure can dynamically stabilize a steady state with no equilibrium analogue. Specifically, we show that balancing Gilbert damping with a dc drive in the magnetic multilayer depicted in Fig. 1 enables us to stabilize

a spacetime-translation-symmetry-breaking chiral spin-superfluid limit cycle. The resulting superflow provides an emergent nonreciprocal background: long-wavelength magnons of opposite chirality acquire intrinsically asymmetric dispersions and propagate direction-selectively, realizing a spin-superfluid diode. Crucially, the nonreciprocity is flow-borne: it is neither inherited from built-in structural asymmetries nor reliant on fine-tuned balancing of coherent and dissipative interactions – it originates from the broken Galilean invariance.

We further establish a concrete analogue-gravity link by showing that, in the comoving, corotating frame of the spin-superfluid limit cycle, phase fluctuations satisfy a scalar wave equation with an effective (1+1)D acoustic metric. The chiral background parametrically squeezes magnons into a stationary two-mode squeezed state. Introducing a current-modulation junction nucleates a sonic horizon across which one mode tunnels by particle-hole pair production while its negative-energy partner is advected, yielding Hawking-like emission bursts.

Taken together, our results elevate a seemingly mundane magnetic heterostructure to a platform in which spin superfluidity, emergent nonreciprocity and Hawking-like emission can be generated, tuned, and diagnosed with standard instrumentation.

Model.—Our starting point is a heterostructure comprising N ferromagnetic layers separated by metallic spacers of thickness a, which mediate an effective RKKY-like exchange A and Dzyaloshinskii–Moriya D interactions (DMI) between neighboring layer magnetizations \mathbf{m}_j and $\mathbf{m}_{j\pm 1}$. An external magnetic field $\mathbf{B} = B\hat{\mathbf{z}}$ aligns the static equilibrium magnetization along the $\hat{\mathbf{z}}$ axis. Each layer obeys Landau–Lifshitz–Gilbert (LLG) dynamics characterized by an intrinsic Gilbert damping

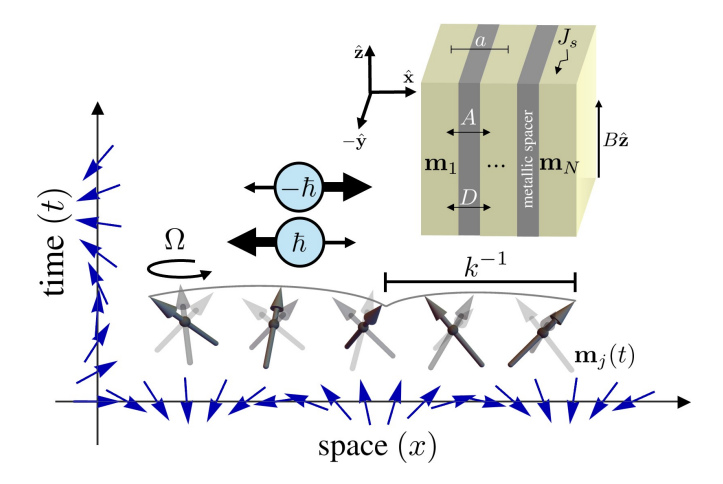


FIG. 1. A schematic depiction of the superfluid limit cycle (SFLC) state realized in our model and the resulting spinwave dynamics. The state breaks both spatial and temporal translation symmetry and supports excitations of opposite angular momenta with asymmetric propagation speeds. Inset: a schematic of the heterostructure device wherein the SFLC can be realized. Each ferromagnetic layer is subjected to the applied field $B\hat{\mathbf{z}}$ and separated by a metallic spacer that mediates both interfacial symmetric and antisymmetric (DM) exchange A and D, respectively. An antidamping torque of strength J_s counteracts the intrinsic dissipation of the magnetization dynamics.

 α and a (antidamping) Slonczewski torque generated via a dc spin current $\mathbf{J}_s = J_s \hat{\mathbf{z}}$. Heterostructures hosting such interactions have been both explored theoretically and realized experimentally [31–38].

To make our analysis physically transparent, we adopt a continuum description, coarse-graining $\mathbf{m}_{j}(t) = \mathbf{m}(x,t)$, with x=ja. In this limit, the state of the system is described by a spacetime-local unit vector $\mathbf{m}(x,t)$ evolving under the LLG equation

$$\partial_t \mathbf{m} = -\mathbf{m} \times \mathbf{h} + \alpha \mathbf{m} \times \partial_t \mathbf{m} + J_s \mathbf{m} \times (\mathbf{m} \times \hat{\mathbf{z}}), \quad (1)$$

where time is measured in units of the characteristic precession frequency $\omega = \gamma B$, with γ the gyromagnetic ratio. The dimensionless effective field $\mathbf{h} = -\delta \tilde{F}/\delta \mathbf{m}$ is derived from the continuum free energy functional $F[\mathbf{m}] = BM_s\tilde{F}[\mathbf{m}]$, with M_s the saturation magnetization and

$$\tilde{F} = \int \left(\frac{1}{2}|D_x \mathbf{m}|^2 + \frac{d^2}{2}(m^{z^2} - 1) - m^z\right) dx, \qquad (2)$$

the dimensionless free energy. Here, $D_x \mathbf{m} = \partial_x \mathbf{m} + d\hat{\mathbf{z}} \times \mathbf{m}$ is a covariant derivative associated with an effective U(1) gauge field of strength $d = \ell_B/\ell_D = D/(AM_sB)^{1/2}$, where $\ell_B = (A/M_sB)^{1/2}$ and $\ell_D = A/D$ associated with the (renormalized) exchange strength A > 0 and DMI strength $D \in \mathbb{R}$. We have also rescaled $x \mapsto \ell_B x$. This covariant formulation of the DMI reveals that, in a frame cospiralling with the DMI-imposed twist (wherein

 $D_x \mapsto \partial_x$), the magnetization experiences an effective anisotropy of strength $d^2/2$ favoring $\mathbf{m} \perp \hat{\mathbf{z}}$ [39–42].

While the model has a global U(1) symmetry about $\hat{\mathbf{z}}$, it lacks a local one: under a position-dependent rotation by an angle $\varphi(x)$ about $\hat{\mathbf{z}}$, the DMI acts as a background gauge potential that transforms as $d \mapsto d + \partial_x \varphi$, thus exhibiting the minimal-coupling structure familiar from superfluid helimagnets [43, 44]. Writing $\mathbf{m} = (\sqrt{1 - m^{z^2}} \cos \phi, \sqrt{1 - m^{z^2}} \sin \phi, m^z)$, global U(1) symmetry yields the conserved Noether current

$$j(x) = D_x \mathbf{m} \cdot (\hat{\mathbf{z}} \times \mathbf{m}) = (1 - m^{z^2})(\partial_x \phi + d).$$
 (3)

Equation (3) defines the spin-superfluid current carried by the azimuthal phase ϕ . In equilibrium, the free energy (2) admits stationary states with uniform current j(x) = j_0 corresponding to spiral states (SSs) of pitch $\partial_x \phi =$ k and $m^z = -1/f_k$, with $f_k = k(k+2d)$ the effective stiffness associated with a spiral of pitch k. These SSs are thus entirely specified by k.

Sufficiently large DMI renders some spiral states energetically stable, as shown by the equilibrium phase diagram in Fig. 2. Specifically, we find that the stable uniform-current states emerge as low-energy spiral states (LESSs) whenever |d| > 1 with the LESS of pitch k = -d serving as the ground state (see Appendix A). Yet echoing the proposals for spin superfluidity in easy-plane collinear magnets [43, 45–47] – an unambiguous equilibrium realization remains experimentally elusive, suggesting that this current-carrying state is difficult to stabilize as a true ground state. We therefore adopt a dynamical approach: by counteracting damping with a dc drive, we seek to stabilize the same current-carrying configuration as a limit cycle in the regime |d| < 1, placing the emergence of spin superfluidity within experimental reach.

To make this concrete, we search for steady, current-carrying solutions of Eq. (1). Introducing the canonically conjugate variables (m^z, ϕ) allows us to recast the dynamics in hydrodynamic form, yielding the coupled non-linear equations

$$\partial_t m^z + \partial_x j = (1 - m^{z^2})(\alpha \partial_t \phi - J_s), \qquad (4a)$$

$$\partial_t \phi = -\frac{\delta \tilde{F}}{\delta m^z} - \alpha \frac{\partial_t m^z}{1 - m^{z^2}}.$$
 (4b)

Equation (4a) is naturally interpreted as a local spincontinuity law: the divergence of the spin current balances nonconservative torques, with J_s and $\alpha \partial_t \phi$, respectively, injecting and dissipating spin angular momentum. For a spatially uniform longitudinal component, i.e., $\partial_x m^z = 0$, Eq. (4b) reduces to

$$\partial_t \phi = 1 + m^z f_\phi - \alpha \frac{\partial_t m^z}{1 - m^{z^2}}, \qquad (5)$$

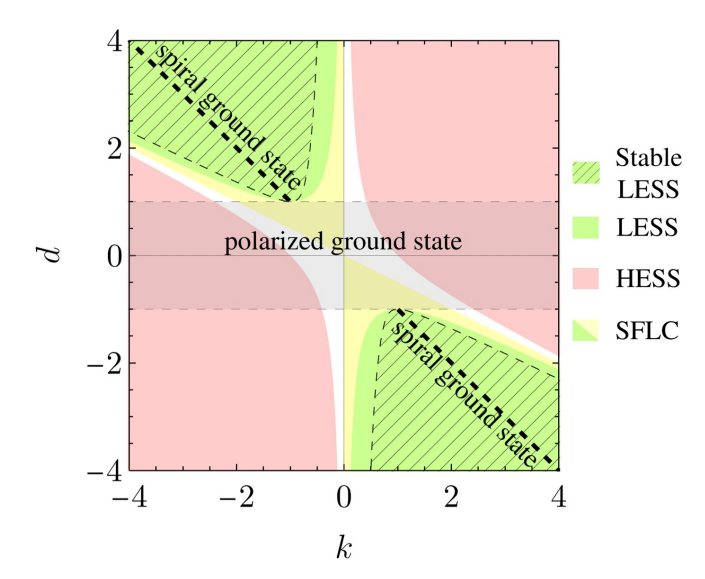


FIG. 2. The equilibrium phase diagram of the model in Eq. (2) superimposed with that of the SFLC. Given a dimensionless DMI d and spiral pitch k, the color of the corresponding region indicates the existence (or non-existence) of either an energetically stable LESS (hatched green), an unstable LESS (unhatched green), or a HESS (red) - which are always unstable (see Appendix A for more details). The grayed out region corresponds to |d| < 1 whereby the ground state is fully polarized $\mathbf{m} = \hat{\mathbf{z}}$. Outside of this region, the ground state is the stable LESS with pitch k = -d indicated with the black dashed line. The yellow/green region corresponds to those values of d (and corresponding values of k) where an SFLC of pitch k can be stably supported. Crucially, the yellow region extends to the weak-DMI regime |d| < 1 where equilibrium superfluid states are forbidden.

where $f_{\phi} = (\partial_x \phi)(\partial_x \phi + 2d)$ is the phase-stiffness density associated with a twist in ϕ . Equations (4a) and (4b) admit a uniformly precessing steady-state *limit-cycle (LC)* solution defined by

$$\phi_{\rm LC}(x,t) = kx + \Omega t$$
, $m_{\rm LC}^z = \frac{\Omega - 1}{f_k}$, (6)

where $\Omega = J_s/\alpha$ is the precession frequency. In this state, the linear phase winding generates a steady, nonzero flow of spin angular momentum, i.e., the spin supercurrent $j_k = n_k v_k$, with $n_k = 1 - m_{\rm LC}^z$ and $v_k = k + d$ defining the spin-superfluid density and velocity, respectively. This nonequilibrium spin superfluid LC (SFLC) phase is well-defined provided that $|m_{\rm LC}^z| < 1$, a condition generically met by a suitable choice of Ω for any $k \neq 0, -2d$. Importantly, no restriction (other than $d \neq 0$) is placed on the DMI strength d, thus extending the regime of realizable stable superfluid states beyond what is possible in equilibrium (see Fig. 2).

Symmetry-wise, the SFLC solution (6) is highly nontrivial: it dynamically breaks rotational, spatial, and continuous time-translation symmetries, exhibiting hallmarks of spacetime-crystalline order intertwined with superfluid transport [48–50]. In particular, continuous space- and time-translational symmetries are broken down to discrete ones with periodicities $2\pi/k$ and $2\pi/\Omega$, respectively. The three broken symmetries, however, are not independent: the original 3-parameter symmetry group is broken down to a single 2-parameter symmetry transformation $(x,t,\phi)\mapsto (x+a,t+\tau,\phi-ka-\Omega\tau)$. Consequentially, only 3-2=1 Goldstone mode emerges associated with azimuthal phase fluctuations $\phi\mapsto\phi+\delta\phi$. The SFLC thus realizes a nonequilibrium incarnation of the so-called "inverse Higgs mechanism", whereby the number of Goldstone modes is not equal to the number of broken symmetries [51].

The state is chiral: the phase propagates unidirectionally with velocity $-\Omega/d$, whose sign is set by d. Its existence, however, does not guarantee its dynamical stability: trajectories nearby need not converge to the solution. To identify the stable sector and the fluctuation spectrum, we proceed to linearize the dynamics about this chiral SFLC background.

Stability and excitations of the SFLC state — In contrast to the usual equilibrium expansion, our background is an explicitly nonequilibrium limit cycle that breaks rotational, spatial, and continuous time-translation symmetry. To handle its complexity, we introduce a unwinding map that flattens the SFLC into a time-independent uniform polarized state amenable to conventional spinwave analysis. Specifically, we perform a spacetime-local SO(3) transformation $\mathbf{n}(x,t) = \mathbf{R}(x,t)\mathbf{m}(x,t)$ with

$$\mathbf{R}(x,t) = \mathbf{R}_{u}(-\theta_{LC})\mathbf{R}_{z}(-kx)\mathbf{R}_{z}(-\Omega t), \qquad (7)$$

where $\mathbf{R}_{\mu}(\theta)$ is the rotation matrix by an angle θ about the μ 'th Cartesian axis and $\cos\theta_{\mathrm{LC}} = m_{\mathrm{LC}}^z$. If $\mathbf{m}_{\mathrm{LC}}(x,t)$ is the SFLC in vector form, then, by construction, $\mathbf{n}_{\mathrm{LC}}(x,t) = \mathbf{R}(x,t)\mathbf{m}_{\mathrm{LC}}(x,t) = \hat{\mathbf{z}}$. Figure 3 illustrates the unwinding map defined by Eq. (7). First, the dynamical rotation $\mathbf{R}_z(-\Omega t)$ freezes the uniform precession; next, the spatial unwinding $\mathbf{R}_z(-kx)$ unwinds the spatial helix; finally, the global tilt $\mathbf{R}_y(-\theta_{\mathrm{LC}})$ aligns the magnetization with the north pole. In the comoving, corotating frame, the LLG equation (1) and the free energy (2) can be recast in terms of the transformed magnetization $\mathbf{n}(x,t)$ via the substitutions:

$$\hat{\mathbf{z}} \mapsto \hat{\mathbf{z}}', \quad \partial_t \mapsto \partial_t + \Omega \hat{\mathbf{z}}' \times, \quad D_x \mapsto \partial_x + (k+d) \hat{\mathbf{z}}' \times,$$
(8)

where $\hat{\mathbf{z}}' = \mathbf{R}_y(-\theta_{\mathrm{LC}})\hat{\mathbf{z}}$ (shown in Fig. 3(b)). The first replacement fixes the tilted quantization axis set by the global y-rotation; the latter two encode the corotating/comoving $\mathfrak{so}(3)$ gauge potential generated by $\mathbf{R}(x,t)$, i.e., $(A_t, A_x) = (\Omega \hat{\mathbf{z}}' \times, k \hat{\mathbf{z}}' \times)$. The transformation (8) leads to the rescaling

$$d \mapsto d + k, \quad J_s \mapsto J_s - \alpha \Omega = 0.$$
 (9)

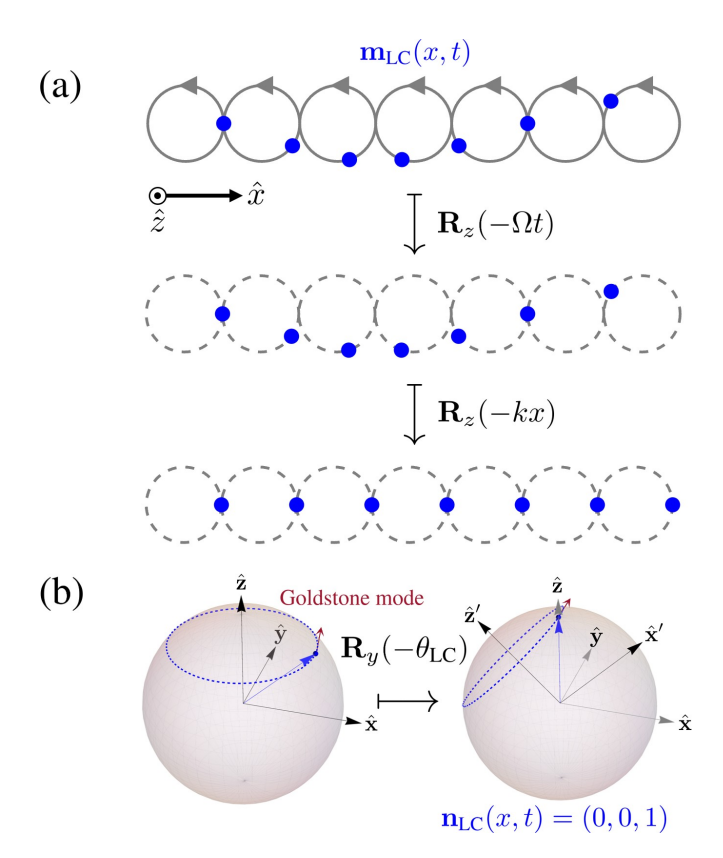


FIG. 3. The SFLC unwinding map defined by Eq. (7). (a) The transverse components of $\mathbf{m}_{\mathrm{LC}}(x,t)$ are shown in blue. The relative spatial variations are set by the SFLC pitch k. The gray arrow indicates the precessing dynamics at frequency Ω of the SFLC state. The first step of the unwinding map moves the system into a frame rotating at Ω , rendering each spin stationary. The second step unwinds the spatial spiral of pitch k. (b) The magnetization is finally globally rotated so that the canted state (with polar angle $\cos\theta_{\mathrm{LC}}=m_{\mathrm{LC}}^z$) is aligned along the north pole. The Goldstone mode associated with phase fluctuations $\phi\mapsto\phi+\delta\phi$ maps onto transverse fluctuations $n^y\mapsto n^y+\delta\phi\sin\theta_{\mathrm{LC}}$, indicated by a red arrow.

Interestingly, Eq. (9) identifies k = -d (corresponding to the LESS ground state in the strong DMI regime) as a gauge-neutral point: in the comoving frame the spatial $\mathfrak{so}(3)$ gauge field $A_x \propto (k+d) \hat{\mathbf{z}}' \times$ vanishes, the DMI shift cancels $(d \to d + k = 0)$, and the superflow velocity is zero $(v_k = k + d = 0)$, rendering the system equivalent to an achiral easy-plane ferromagnet. Importantly, under Eq. (7), the Goldstone mode associated with azimuthal phase fluctuations maps onto the transverse component n^y which transforms as $n^y \mapsto n^y + \delta \phi \sin \theta_{\rm LC}$ under $\phi \mapsto \phi + \delta \phi$ (see Appendix C).

Linearizing about the unwound background, we write $\mathbf{n} = \hat{\mathbf{z}} + \delta \mathbf{n}$ and define $\psi = \delta n^x + i \, \delta n^y$. In this frame, the original U(1) symmetry axis is shifted $\hat{\mathbf{z}} \mapsto \hat{\mathbf{z}}'$ (see Fig. 3(b)). Consequently, the quadratic theory about the new $\hat{\mathbf{z}}$ is not number-conserving and dynamically couples ψ with ψ^* . The fluctuation dynamics are therefore

naturally cast in Bogoliubov-de Gennes (BdG) form:

$$i(\mathbb{1}_2 - i\alpha\sigma_3)\partial_t\Psi_a = \mathbf{G}_a\Psi_a,\tag{10}$$

where $\Psi_q=(\psi_q,\psi_{-q}^*)$ is the momentum-space Nambu spinor [52] of fluctuations, σ_j are the Pauli matrices, and

$$\mathbf{G}_{q} = -2m_{\mathrm{LC}}^{z} v_{k} q \mathbb{1}_{2} + (\Delta_{k} - q^{2}) \boldsymbol{\sigma}_{3} + \Delta_{k} i \boldsymbol{\sigma}_{2}, \quad (11)$$

where $\Delta_k = f_k n_k/2$ is the effective pairing strength, i.e., a parametric drive of particle-hole pairs. The effective BdG Hamiltonian \mathbf{G}_q is pseudo-Hermitian with respect to σ_3 , i.e., $\mathbf{G}_q^{\dagger} = \sigma_3 \mathbf{G}_q \sigma_3$, reflecting the bosonic nature of magnonic excitations [53]. Additionally, it satisfies the "particle-hole" constraint $\mathbf{G}_q^* = -\sigma_1 \mathbf{G}_{-q} \sigma_1$ [54]. Thus, in the formal limit where the dissipative term on the left-hand side of Eq. (10) is set to zero, the nonequilibrium dynamics are effectively coherent.

Owing to the BdG structure of Eq. (10), the normal modes (eigenvectors) of \mathbf{G}_q naturally split into particle-like and hole-like sectors. This separation becomes precise upon quantization, with $\psi_q \mapsto \sqrt{2s}\,\hat{a}_q$ ("carrying \hbar ") and $\psi_{-q}^* \mapsto \sqrt{2s}\,\hat{a}_{-q}^\dagger$ ("carrying $-\hbar$ ") in terms of magnon annihilation and creation operators. These sectors are distinguished by the Krein signature κ of the corresponding eigenvector, defined as the sign of the indefinite inner product $\vec{v}^\dagger \boldsymbol{\sigma}_3 \vec{v}$ [55–58]. In our convention, $\kappa = -1$ (+1) corresponds to the particle (hole) band [59]. The particle-band dispersion takes the form

$$\omega_p(q) = -2m_{\text{LC}}^z v_k q + |q| \sqrt{q^2 - 2\Delta_k}$$

$$\approx \begin{cases} c_- q, & q < 0, \\ c_+ q, & q > 0, \end{cases}$$
(12)

where $c_{\pm} = -2m_{\rm LC}^z v_k \pm \sqrt{-2\Delta_k}$ is the sound velocity of the right- (left-) moving branch with respect to q=0. The hole band is related by $\omega_h(q)=-\omega_p(-q)$ via the particle-hole constraint. Proceeding under the assumption $\Delta_k < 0$, or equivalently $v_k^2 < d^2$, we thus uncover generically asymmetric, nonreciprocal dispersion $(c_{+} \neq -c_{-})$ for excitations of negative and positive momenta. In the lab frame, this corresponds to excitations of momentum q < -k and q > -k, respectively. In Fig. 4(a) we plot an asymmetry measure c_++c_- throughout the region of SFLC parameter space where $\Delta_k < 0$. This measure vanishes (indicating symmetric dispersion) only when $\Omega = 1$, wherein the SFLC is resonant with the applied field, or k = -d corresponding to the zero velocity SFLC background. The sound velocities c_{+} are plotted in Fig. 4(b) while varying the SFLC frequency at a fixed pitch. In Figs. 4(c-g), the long-wavelength dispersion is plotted for various choices of Ω with clear asymmetry visible in all cases except for (e) where $\Omega = 1$.

Remarkably, there even exist regimes where the long-wavelength dynamics are completely unidirectional:

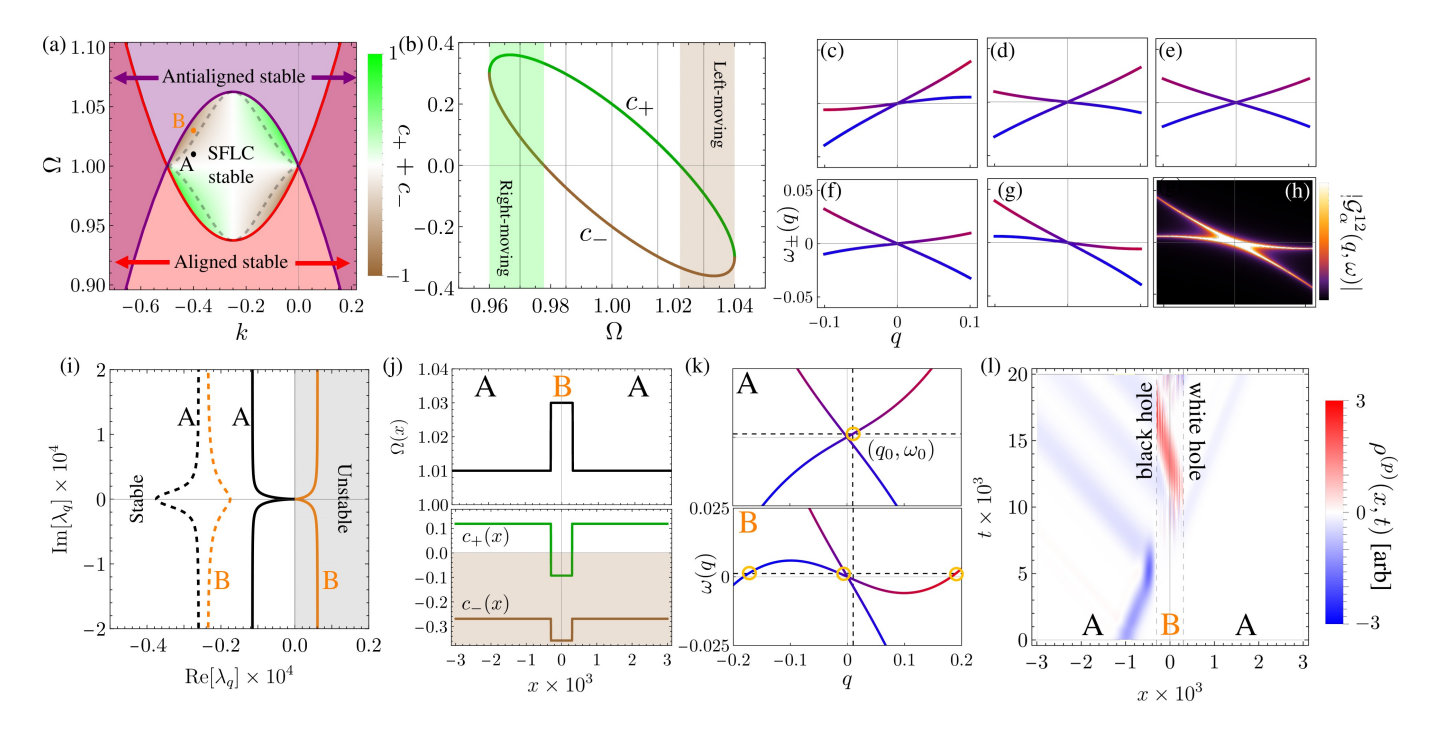


FIG. 4. (a) Wave-propagation asymmetry $c_+ + c_-$ plotted throughout the SFLC stability phase diagram. The central region bounded by gray dashed lines indicates the set of drive strengths $J_s = \alpha \Omega$ and pitches k where an SFLC is stably supported. Regions bounded by the purple/red lines and the dashed boundaries correspond to parameter sets where only the Goldstone mode is unstable, or equivalently, long-wavelength spin waves on top of the SFLC propagate unidirectionally. If $(k, J_s/\alpha)$ is in the red (purple) region, a spin-wave of momentum k will relax toward the aligned (antialigned) state $\mathbf{m} = +\hat{\mathbf{z}} \ (-\hat{\mathbf{z}})$; in the overlapping region, the final steady state depends on the initial canting angle. The black (A) and orange (B) markers indicate the parameter choices used in panels (i-l). (b) Sound velocities c_{\pm} defined below Eq. (12) versus SFLC frequency Ω ; green (brown) curves correspond to c_+ (c_-), with shaded regions highlighting right- (left-)propagating unidirectional regimes. (c-g) Magnon dispersion atop the SFLC of pitch k = -0.4 for $\Omega = 0.97, 0.985, 1, 1.015, 1.03$ (increasing left to right). (h) Anomalous correlator strength defined below Eq. (13) for the Ω of (g). (i) Complex eigenvalue bands $\lambda_q^{(1)}$ (solid) and $\lambda_q^{(2)}$ (dashed) of the dynamical matrix \mathbf{M}_q defined above Eq. (15), plotted for $q \in [-0.1, 0.1]$. The color of each band corresponds to the SFLC parameters A and B in (a). (j) Spatial profiles of the local SFLC frequency and sound velocities in the scattering scenario considered, using the same color code as in (b). (k) Dispersion within regions A (top) and B (bottom) of the scattering geometry of (j). The color coding matches that in (c-g). The vertical (horizontal) dashed line indicates the momentum q_0 (frequency $\omega_0 = \omega_p(q_0)$) used for the initial condition Eq. (20). The yellow circle in A encloses (q_0, ω_0) , while the three yellow circles in B identify the intersections of ω_0 with the dispersion curves in region B, corresponding to the frequency-allowed scattering channels. (1) Wavepacket scattering visualized using the particle pseudocharge density defined in Eq. (21). For (a-l), d = 0.25 and, in (i,l), $\alpha = 10^{-3}$. In (k-l), horizons are located at $\pm x_0 = \pm 200$. The initial condition used in (l) is defined in and around Eq. (20) with $q_0 = 0.01$ with χ being a Gaussian centered at $x_0 = -1000$ and characteristic width 200.

 $c_+c_->0$, shown as green and brown regions of Fig. 4(b). In these regimes, both the particle and hole bands become negative on one side of q=0. While in conventional bosonic systems this would indicate a thermodynamic (or Landau) instability [57, 60], it does not in this model. That is because the nonequilibrium SFLC background sets an effective "Fermi level" at Ω in the lab frame: negative energy excitations represent lab-frame excitations of positive frequencies just below Ω .

Unlike the non-Hermitian skin effect, which relies on asymmetric hopping [61–63] (typically induced by a precise combination of coherent and incoherent interaction [30, 38, 64]), the nonreciprocity discussed here arises even though \mathbf{G}_q generates coherent dynamics with strictly reciprocal couplings. Its origin is the directed motion

of the SFLC background, which breaks Galilean invariance: i.e., transforming to the frame comoving with the superflow (effectively setting $v_k=0$ in Eq. (12)) does not halt magnon propagation. This behavior is characteristic of uniform hydrodynamic states (UHSs) [65], of which the SFLC is a concrete example. Prior discussions confined boost-noninvariant UHSs to undriven, lossless limits, with damping merely curtailing lifetime. Here, inversion-symmetry-breaking DMI, together with a compensating dc drive, stabilizes a manifold of fully stable and locally attractive UHSs — a bona fide nonequilibrium phase rather than a fine-tuned transient.

An eigenmode analysis of \mathbf{G}_q reveals further insights. At q = 0 the particle and hole bands coalesce at an exceptional point (EP) with \mathbf{G}_0 possessing one eigenvector $\propto [i,-i]$. For $\psi_0 = i$, we have $\delta n^x = 0$ and $\delta n^y = 1$, physically corresponding to a uniform y-tilt of **n** that advances **m** along the SFLC orbit without changing the pitch. This is the Goldstone mode previously identified with azimuthal phase fluctuations in the lab-frame magnetization **m** (see Fig. 3(b) and Appendix C). For $q \neq 0$, \mathbf{G}_q is diagonalizable with two modes whose Nambu (particle-hole) weights continuously approach equal modulus as $q \to 0$, as shown in Figs.4(c-g). The mixing is captured by the Green's function

$$\mathcal{G}(q,\omega) = (\omega \mathbb{1}_2 - \mathbf{G}_q)^{-1},\tag{13}$$

whose off-diagonal component $\mathcal{G}^{12}(q,\omega)$ measures the anomalous (pair) amplitude. Figure 4(h) shows that the anomalous amplitude peaks at the Goldstone point $(\omega,q)=(0,0)$: the SFLC background acts as a parametric pump that mixes particles and holes, generating long-wavelength correlated (q,-q) pairs with, in the quantum regime, two-mode-squeezed statistics.

We now assess the stability of the eigenmodes by analyzing the dynamical matrix $\mathbf{M}_q = -i(\mathbb{1}_2 - i\alpha\boldsymbol{\sigma}_3)^{-1}\mathbf{G}_q$, defined implicitly by rearranging Eq. (10) into the form $\partial_t \Psi_q = \mathbf{M}_q \Psi_q$. A mode fluctuation is dynamically stable when Re $\lambda_q < 0$ for its eigenvalue λ_q . At q = 0 the two eigenvalues satisfy

$$\operatorname{Re} \lambda_0^{(1)} = 0, \qquad \operatorname{Re} \lambda_0^{(2)} = \frac{2\alpha \,\Delta_k}{1 + \alpha^2}.$$
 (14)

The first, infinite-lifetime, mode is the Goldstone mode which survives in the presence of dissipation. The second mode is stable only when $\Delta_k < 0$ - the same condition already noted for dynamical stability of the coherent dynamics generated by \mathbf{G}_q . For small but nonzero q, the second mode remains damped for $\Delta_k < 0$, while the Goldstone mode acquires a perturbative decay rate:

Re
$$\lambda_q^{(1)} \approx -\frac{2(m_{\rm LC}^z v_k)^2 + \Delta_k}{\alpha \Delta_k} q^2 = \frac{4c_+ c_-}{\alpha (c_+ - c_-)^2} q^2$$
. (15)

Local stability around q=0 requires the coefficient of q^2 in Eq. (15) to be negative, which translates into the condition $c_+c_-<0$. In this regime, a local phase twist can decompose into left- and right-moving packets that spread and decay under Gilbert damping. On the other hand, in the unidirectional regime $c_+c_->0$, phase twists cannot disperse by counter-propagation; the anomalous coherence pumped by the SFLC then accumulates, and the Goldstone mode rate changes sign, signaling a parametric instability. In the following, we will show that the stable-to-unstable transition at $c_+c_-=0$ can be also understood as the kinematic fingerprint of black-hole horizon, with Hawking-like pair production.

Long-wavelength analogue black hole horizons— To make the analogue-gravity parallel explicit, we recast the long-wavelength dynamics in an acoustic-metric form. In the long-wavelength limit, the Goldstone mode δn^y (or

equivalently in the lab-frame $\delta \phi$ - see Appendix C) obeys the hyperbolic wave equation

$$(\partial_t - c_- \partial_x)(\partial_t - c_+ \partial_x)\delta n^y = 0, \qquad (16)$$

whose characteristics correspond to the null trajectories of the effective spacetime line element

$$ds^{2} = c_{+}c_{-}dt^{2} - (c_{+} + c_{-})dxdt + dx^{2}.$$
 (17)

Equation (17) reveals two main intertwined kinematic knobs: (i) the product c_+c_- fixes the light-cone opening and flips sign at a horizon ($c_{\pm}=0$), marking the transition from bi- to unidirectional propagation; (ii) the shift term $c_+ + c_- \propto v_k$ encodes flow-induced frame dragging by the chiral superfluid background.

These observations motivate an analogue-gravity construction in which Hawking-like emission in a tabletop magnet is realized by spatially modulating the spin-transfer torque. To make this concrete, we consider the scattering geometry depicted in Fig. 4(j). A smooth profile $J_s(x)$ – and thus $\Omega(x) = J_s(x)/\alpha$ – imprints position dependence on the sound speeds $c_{\pm}(x)$ and selects locations $x = \pm x_0$ where the right-moving branch closes, $c_{+}(\pm x_{0}) = 0$, establishing sonic horizons that separate propagation regimes. Outside $|x| > x_0$ (region A), $J_s(x) \approx J_s^A$ is nearly constant and tuned to the bidirectional phase with $c_{+}(x)c_{-}(x) < 0$; inside $|x| < x_{0}$ (region B), $J_s(x) \approx J_s^B$ is nearly constant and tuned to the unidirectional phase with $c_{+}(x)c_{-}(x) > 0$. At the interfaces $x = \pm x_0$, we take $J_s(x)$ to smoothly interpolate between J_s^A and J_s^B over a characteristic length scale l.

Suppose Eq. (1) admits a solution that supports, within region A (B), an SFLC with pitch k_A (k_B) and frequency $\Omega_A = J_s^A/\alpha$ ($\Omega_B = J_s^B/\alpha$) with dynamical domain walls in the interfacial regions. In such a scenario, magnon transport can be analyzed by suitably generalizing Eq. (10). In real space, the equation of motion reads

$$i(\mathbb{1}_2 - i\alpha\sigma_3) \partial_t \Psi(x, t) = \mathbf{G}(x)\Psi(x, t),$$
 (18)

where $\mathbf{G}(x)$ is obtained from \mathbf{G}_q in Eq. (11) by replacing $q \mapsto -i\partial_x$ and $J_s \mapsto J_s(x)$. Explicitly, with $k_{A,B} = k$,

$$\mathbf{G}(x) = \Delta_k(x)(\boldsymbol{\sigma}_3 + i\boldsymbol{\sigma}_2) + 2im_{\mathrm{LC}}^z(x)v_k \mathbb{1}_2 \partial_x + \boldsymbol{\sigma}_3 \partial_x^2.$$
(19)

It is important to note that the above equation is exact only when the SFLC precesses locally at $\Omega(x) = J_s(x)/\alpha$, in which case it must be interpreted pointwise in a frame rotating at $\Omega(x)$. Rapid spatial variations of $J_s(x)$ generate additional, non-negligible terms from the position-dependent rotation $\mathbf{R}_z[-\Omega(x)t]$ in the unwinding map Eq. (7), i.e., $\propto \partial_x \Omega$, which are neglected here. Thus, our analysis is valid everywhere except within a narrow interfacial region. In this spatially adiabatic regime, a component of $\Psi(x,t) \propto \chi_\omega(x)e^{-i\omega t}$ localized near x corresponds in the lab frame to an excitation at frequency $\Omega(x) + \omega$ -that is, ω always represents a local detuning.

To understand scattering dynamics, within each A/B region, we can define the momentum-space BdG Hamiltonian $\mathbf{G}_q^{A/B} = \mathbf{G}_q \big|_{J_s = J_s^{A/B}}$, whose spectra are shown in Fig. 4(k). Due to time-translation invariance of Eq. (18) (implying frequency conservation), an incident right-moving particle mode with momentum $q_0 > 0$ and frequency $\omega_0 = \omega^{(p),A}(q_0) > 0$ (dashed lines in dispersion A) can only scatter into (i) long-wavelength left-moving particle and hole states (central yellow circle in dispersion B) or (ii) short-wavelength right-moving particle and hole states (left- and rightmost yellow circles in dispersion B).

To test the acoustic-metric picture of Eqs. (16)-(17), we launch a right-moving, long-wavelength wave packet from the left asymptotic region $(x \ll -x_0)$ with central momentum $q_0 \ll 1$. Specifically, we write $\Psi(x,0) = \Psi^{(p)}(x) + \Psi^{(h)}(x)$ where the particle component is given by

$$\Psi^{(p)}(x) = \chi(x)e^{iq_0x}\mathbf{u}_{q_0}^A, \qquad (20)$$

with $\chi(x)$ a Gaussian localized at $x=x_0\ll -x_0$ and $\mathbf{u}_{q_0}^A$ is the eigenvector of \mathbf{G}_q^A at $q=q_0$ with frequency $\omega_p(q_0)>0$ satisfying the pseudo-Hermitian normalization $\mathbf{u}_{q_0}^{A\dagger}\boldsymbol{\sigma}_3\mathbf{u}_{q_0}^A=-1$. Reality of δn^x and δn^y fixes the hole partner as $\Psi^{(h)}=\boldsymbol{\sigma}_1\Psi^{(p)}(x)^*$. Linearity allows us to evolve the particle and hole components independently and the relationship $\mathbf{G}^*(x)=-\boldsymbol{\sigma}_1\mathbf{G}(x)\boldsymbol{\sigma}_1$ guarantees $\Psi^{(h)}(x,t)=\boldsymbol{\sigma}_1\Psi^{(p)}(x,t)^*$ for all $t\geq 0$.

As a quantitative witness to particle-hole dynamics, we define the particle pseudocharge density

$$\rho^{(p)}(x,t) = \Psi^{(p)\dagger}(x,t)\sigma_3\Psi^{(p)}(x,t). \tag{21}$$

For our initial state, $\rho^{(p)}(x,0) = -\chi^2(x)$. In general, $\rho^{(p)}(x,t) < 0 > 0$ indicates a concentration of particles (holes) at (x,t) and it flips sign only when particle—hole correlations are generated (see Appendix B).

Figure 4(1) shows the evolution of $\rho^{(p)}(x,t)$ corresponding to the scattering of the Gaussian wavepacket with particle component Eq. (20) through the geometry depicted in Fig. 4(j). Initially, the long-wavelength particle density (blue color) propagates toward the black-hole horizon with group velocity $\left. d\omega_p/dq \right|_{q=q_0} > 0$. At the horizon, long-wavelength particles are unable to tunnel and instead weakly scatter into right-moving higher momentum particle and hole channels within region B. Upon reaching the white-hole horizon, these modes split: a portion reflects as long-wavelength holes back into region B, while the remainder transmits as long-wavelength particles into region A. The black-hole-white-hole pair thus forms a black-hole-laser cavity that repeatedly squeezes the (q, -q) pair, generating quasi-periodic, Hawking-like particle bursts into the left-half of region A accompanied by sign reversals of $\rho^{(p)}$ that mark particle \leftrightarrow hole conversion. In parallel, a faint, phase-coherent thread of low-q particles traverses B and emerges into the right half of A a BdG Klein-tunneling analogue.

Several recent studies have proposed magnetic analogues of curved spacetime and relativistic scattering, including magnonic black holes and Klein tunneling in spintorque-driven or chiral magnetic media. Early proposals demonstrated that a uniform current can Doppler-shift magnon modes to create spin-flow horizons when the drift velocity equals the spin-wave speed [66], while subsequent works explored interface-based antimagnonic amplification [67], lattice analogues of Dirac fields on curved backgrounds [68], cavity-like black-hole lasing driven by strong spin torques in patterned waveguides [69], and even spin-superfluid analogues in superfluid ³He-B [70]. These approaches rely on externally imposed currents or engineered inhomogeneities to kinematically generate horizon conditions within near-equilibrium magnets. By contrast, our mechanism embeds the analogue-gravity physics inside a self-organized nonequilibrium phase: the chiral SFLC arises dynamically from the interplay between drive and damping, producing an intrinsically nonreciprocal background. A smooth spatial modulation of the spin torque then maps onto an acoustic metric and creates sonic horizons—without externally provided flows or fragile gain-loss fine-tuning. This selfoscillatory route unifies nonreciprocity, analogue gravity, and driven-dissipative phases within a single, experimentally transparent magnetic platform.

Discussion— We have shown that a conventional multilayer ferromagnet, operated under a steady spin-torque drive, supports a chiral spin-superfluid limit cycle that spontaneously breaks continuous time and space translations and endows long-wavelength magnons with an intrinsically nonreciprocal dispersion. In the comoving, corotating frame, the linearized dynamics are pseudo-Hermitian, and the long-wavelength Goldstone mode obeys a scalar wave equation with a (1+1)D acoustic metric. Spatially patterned drives thus act as a kinematic control knob for sonic horizons and Bogoliubov mixing, enabling Hawking-like particle—hole pair production.

Mechanistically, the nonreciprocity is flow-borne: it originates from the directed SFLC background and the concomitant breaking of Galilean invariance, not from asymmetric couplings or fragile gain—loss balance. This separates our diode effect from phenomena such as the non-Hermitian skin effect, where asymmetric hopping is essential. In our case, transforming to the superflow frame does not freeze propagation; the two sound speeds remain distinct, and their product and sum control the "light-cone" opening and effective frame-dragging of the acoustic geometry. The emergence of an exceptional point and a Goldstone mode provide a unified lens on both the time-crystalline-like order and the particle—hole structure of fluctuations.

These kinematic handles translate into practical diagnostics. The flow-set asymmetry of the long-wavelength branches implies direction-selective transmission that can be read out with standard spintronics probes. Enter-

ing the unidirectional regime $c_+c_->0$ pins one chirality and produces threshold-like amplification of correlated (q,-q) pairs – signals that should appear as drive-tunable sidebands, excess low-frequency noise, and phase-sensitive two-mode correlations. In horizon geometries, $\mathrm{SU}(1,1)$ Bogoliubov mixing converts incident long-wavelength particles into high-q modes and back into long-wavelength particle—hole partners, yielding quasiperiodic emission bursts and sign flips of a particle—hole witness (pseudocharge) across the interface. Each of these observables follows directly from the pseudo-Hermitian BdG structure and the acoustic-metric hydrodynamics derived here.

Conceptually, this platform broadens the landscape of nonreciprocal phases and nonequilibrium criticality. Rather than approaching nonreciprocal fixed points via static order and critical exceptional points (CEPs), we reach a chiral, time-crystalline state by a dynamical bifurcation from a steady driven phase, after which spectral topology (i.e., exceptional degeneracies) and hydrodynamics together govern transport. Experimentally, the ingredients are standard – Gilbert damping, interfacial exchange and DMI, and dc spin-current injection – and the key control parameters are transparent. This simplicity suggests immediate routes in sputtered multilayers where interlayer exchange and DMI are already engineered and characterized [36, 71, 72] and the phenomena we predict can be resolved via Brillouin light scattering, broadband ferromagnetic resonance, magnetization-noise and propagating spin-wave spectroscopy [73].

Taken together, these results position magnetic heterostructures as a quantitative testbed for non-equilibrium universality where nonlinearity and non-Hermiticity are independently tunable and experimentally accessible. Furthermore, the emergence of nonreciprocity and a phase Goldstone mode links our system to recently uncovered nonreciprocal transitions at non-Hermitian quantum criticality [11, 12, 18, 19], yet the mechanism is distinct: the transition into the SFLC state is not facilitated through a CEP, nor is it from a static already-symmetry-broken state. These parallels and differences call for a systematic, head-to-head comparison of the two routes to criticality.

Acknowledgments.—The authors would like to thank Lorenza Viola and Michiel Burgelman for fruitful discussions. This work was supported by the Office of Naval Research under Award No. N000142412427.

Appendix A: Equilibrium analysis

In this Appendix we summarize the equilibrium solutions of the functional \tilde{F} defined in Eq. (2). Besides the fully polarized state, $\mathbf{m} = \hat{\mathbf{z}}$ (with dimensionless free-energy density -1), there exists a one-parameter family of spiral configurations with $\phi(x) = kx$ and uni-

form longitudinal component $m^z=-1/f_k$ (admissible for $|f_k|>1$) that satisfy the Euler–Lagrange condition $\delta \tilde{F}/\delta \mathbf{m}=0$. All such states have energy density given by $(f_k+f_k^{-1})/2$. The condition $|f_k|>1$ constrains k to satisfy either (i) $|k+d|<\sqrt{d^2-1}$ or (ii) $|k+d|>\sqrt{d^2-1}$. The former class of states, which exist only for |d|>1, have energy density strictly less than that of the polarized state. These are the LESSs discussed in the main text. Within this class, the LESS with k=-d has the lowest energy. In contrast, states in the latter class always exist and have energy density higher than the polarized state. These are the HESSs discussed in the main text.

To determine the energetic stability of these states, we expand the free energy (2) in fluctuations of the azimuthal angle ϕ and the polar angle $\theta = \arccos m^z$. Expanding around the polarized state $\theta = 0$ leads to fluctuations

$$\delta \tilde{F} = \frac{1}{2} \int \left[(\partial_x \theta)^2 + (f_\phi + 1)\theta^2 \right] dx, \qquad (22)$$

where $f_{\phi} = (\partial_x \phi)(\partial_x \phi + 2d)$ is the free energy density carried by an arbitrary azimuthal profile $\phi(x)$ (which is ill-defined in the polarized equilibrium state). Evidently, the mass gap closes and the polarized state destabilizes when the spiral pitch $\partial_x \phi = k$ satisfies $f_k < -1$, corresponding to LESSs.

The free energy of fluctuations about an arbitrary spiral state, up to constant shifts, reads

$$\delta \tilde{F} = \frac{1}{2} \int \left[(\partial_x \tilde{\theta})^2 - f_k n_k \tilde{\theta}^2 + n_k (\partial_x \tilde{\phi} + v_k)^2 - \frac{4v_k \sqrt{n_k}}{f_k} \tilde{\theta} \partial_x \tilde{\phi} \right] dx , \qquad (23)$$

where $\tilde{\phi} = \phi - kx$ and $\tilde{\theta} = \theta - \arccos(-1/f_k)$ are the fluctuations in ϕ and θ respectively, $n_k = 1 - 1/f_k^2 > 0$ is the superfluid density, and $v_k = k + d$ is the superfluid velocity (such that $j_k = n_k v_k$ is the superfluid current). From left to right, the terms in Eq. (23) correspond to the polar angle stiffness, the polar angle mass term, the azimuthal stiffness in the presence of the effective superfluid gauge field, and a coupling term between the polar field and the azimuthal gradient. As expected, energetic stability requires that $f_k < 0$ (thus excluding stability of HESSs) – but this criterion is only necessary. To obtain a sufficient condition, we move to Fourier space $(\theta(x), \phi(x)) \mapsto \Phi_q = (\theta_q, \phi_q)$ and rewrite Eq. (23) as

$$\delta \tilde{F} = \frac{1}{2} \int \Phi_q^{\dagger} \mathbf{F}_q \Phi_q \, dq + \delta \tilde{F}_{\text{bdry}}, \tag{24a}$$

$$\mathbf{F}_{q} = \begin{bmatrix} n_{k}q^{2} & 2iv_{k}\sqrt{n_{k}}q/f_{k} \\ -2iv_{k}\sqrt{n_{k}}q/f_{k} & q^{2} - f_{k}n_{k} \end{cases}$$
(24b)

where $\delta \tilde{F}_{\text{bdry}}$ is a boundary term due to the gauge field. Energetic stability is equivalent to positive definiteness of the Hermitian matrix \mathbf{F}_q , which implies the following necessary and sufficient conditions for energetic stability of a LESS:

$$f_k < 0 \text{ and } v_k^2 < \frac{n_k |f_k|^3}{4} = \frac{n_k |v_k^2 - d^2|^3}{4}.$$
 (25)

The upper bound on the superflow velocity is known as the Landau criterion for stability of spin superfluids [43]. Figure 2 in the main text shows that some LESSs are energetically unstable. In contrast, the special spiral with k=-d satisfies $v_{k=-d}=0$ and is always energetically stable. Because this configuration also minimizes the energy density within the LESS branch, it is the ground state for |d| > 1.

Appendix B: Pseudocharge conservation for pseudo-Hermitian systems

In this Appendix, we discuss in detail the definition of the particle pseudocharge density $\rho^{(p)}(x,t)$ (21) used to quantify particle-hole dynamics in the scattering scenario discussed in the main text. For a homogeneous antidamping torque profile J_s , the real-space BdG Hamiltonian $\mathbf{G}(x)$ (19) is pseudo-Hermitian with respect to the indefinite inner product $\langle \Psi, \Phi \rangle = \int \Psi^{\dagger}(x) \boldsymbol{\sigma}_3 \Phi(x) dx$. Correspondingly, the local pseudocharge density $\rho(x,t) = \Psi^{\dagger}(x,t) \boldsymbol{\sigma}_3 \Psi(x,t)$ satisfies a continuity equation $\partial_t \rho + \partial_x \mathcal{J} = 0$ with

$$\mathcal{J} = -2im_{LC}^z v_k \Psi^{\dagger} \boldsymbol{\sigma}_3 \Psi - i \left[(\partial_x \Psi^{\dagger}) \Psi - \Psi^{\dagger} (\partial_x \Psi) \right]. \tag{26}$$

When $\mathbf{G}(x)$ depends on position through the spin-current profile $J_s(x)$ as in Eq. (19), the coupling between position and momentum $(-i\partial_x)$ breaks strict pseudo-Hermiticity. Consequently, the continuity law picks up a source: $\partial_t \rho + \partial_x \mathcal{J} = \mathcal{S}(x)$, with $\mathcal{S}(x) \propto J_s'(x)$, signifying that pseudocharge is created or absorbed where $J_s(x)$ varies, e.g., in our case, at the interfaces. For general states, the sign of ρ is tied to particle or hole concentration (with $\rho > 0$ (< 0) indicating particle (hole) concentration), while for physical states obeying the reality constraint $\Psi(x,t) = \sigma_1 \Psi^*(x,t)$, the density vanishes, i.e., $\rho(x,t) = 0$ for all (x,t). The continuity law then reduces to $\partial_x \mathcal{J} = \mathcal{S}(x)$, implying that the integrated source enforces a jump in the pseudocurrent across an interface.

Since we wish to quantify particle-hole dynamics (which $\rho = 0$ trivially cannot bear witness to), we instead use the particle pseudocharge density defined in Eq. (21) which computes ρ for the particle component of a physical state Ψ only.

Appendix C: Mapping lab-frame angle fluctuations to SFLC frame transverse fluctuations

In this Appendix, we relate fluctuations in the labframe azimuthal ϕ and polar θ angles to transverse fluctuations of the SFLC-frame magnetization \mathbf{n} . Recalling the definition of the SFLC density $n_k = 1 - m_{\text{LC}}^z^2 = \sin^2 \theta_{\text{LC}}$, and by expanding both sides of $\mathbf{n}(x,t) = \mathbf{R}(x,t)\mathbf{m}(x,t)$ about the SFLC, we find

$$\delta n^x = \delta \theta, \quad \delta n^y = \sqrt{n_k} \delta \phi,$$
 (27)

where δn^x and δn^y are the transverse fluctuations in \mathbf{n} , $\delta \theta = \theta - \theta_{\mathrm{LC}}$, and $\delta \phi = \phi - \phi_{\mathrm{LC}}$. With this, it becomes natural to associate the real and imaginary quadratures associated with $\psi = \delta n^x + i \delta n^y$ with polar and azimuthal fluctuations, respectively. In particular, the Goldstone mode $\delta \phi$ is simply the imaginary quadrature $\mathrm{Im}[\psi]$ scaled by the SFLC density n_k . The dissipative BdG equation (10) accordingly maps to

$$i(\mathbb{1}_2 + i\alpha \sigma_2)\partial_t \Phi_q = \tilde{\mathbf{G}}_q \Phi_q,$$
 (28)

where $\Phi_q = (\delta\theta_q, \sqrt{n_k}\delta\phi_q)$ and $\tilde{\mathbf{G}}_q = -2m_{\mathrm{LC}}^z v_k q \mathbb{1}_2 + (q^2 - \Delta_k)\boldsymbol{\sigma}_2 - \Delta_k i\boldsymbol{\sigma}_1$ is unitarily equivalent to $\tilde{\mathbf{G}}_q$. When q = 0, for example, $\tilde{\mathbf{G}}_0$ has one eigenvector [0, 1] at zero frequency - the Goldstone mode. In the formal limit $\alpha \to 0$, this system of first-order ODEs (in time) can be mapped onto a single second-order ODE

$$(\partial_t + ic_+ q)(\partial_t + ic_- q)\delta\phi = \mathcal{O}(q^4), \tag{29}$$

which, in the limit $q \to 0$, and under the identification Eq. (27), leads to Eq. (16) in the main text.

- D. R. Chialvo, Emerging complex neural dynamics, Nat. Phys. 6, 744 (2010).
- [2] L. S. Schulman and P. E. Seiden, Percolation and galaxies, Science 233, 425 (1986).
- [3] N. Malossi, M. Valado, S. Scotto, P. Huillery, P. Pillet, D. Ciampini, E. Arimondo, and O. Morsch, Full counting statistics and phase diagram of a dissipative Rydberg gas, Phys. Rev. Lett. 113, 023006 (2014).
- [4] D. Dreon, A. Baumgärtner, X. Li, S. Hertlein, T. Esslinger, and T. Donner, Self-oscillating pump in a topological dissipative atom-cavity system, Nature 608, 494 (2022).
- [5] Q. Fontaine, D. Squizzato, F. Baboux, I. Amelio, A. Lemaître, M. Morassi, I. Sagnes, L. Le Gratiet, A. Harouri, M. Wouters, et al., Kardar-Parisi-Zhang universality in a one-dimensional polariton condensate, Nature 608, 687 (2022).
- [6] L. M. Sieberer, M. Buchhold, J. Marino, and S. Diehl, Universality in driven open quantum matter, Reviews of Modern Physics 97, 025004 (2025).
- [7] S. Diehl, A. Tomadin, A. Micheli, R. Fazio, and P. Zoller, Dynamical phase transitions and instabilities in open atomic many-body systems, Phys. Rev. Lett. 105, 015702 (2010).
- [8] M. Fitzpatrick, N. M. Sundaresan, A. C. Y. Li, J. Koch, and A. A. Houck, Observation of a Dissipative Phase Transition in a One-Dimensional Circuit QED Lattice, Phys. Rev. X 7, 011016 (2017).

- [9] F. Minganti, A. Biella, N. Bartolo, and C. Ciuti, Spectral theory of Liouvillians for dissipative phase transitions, Phys. Rev. A 98, 042118 (2018).
- [10] R. Hanai, A. Edelman, Y. Ohashi, and P. B. Littlewood, Non-hermitian phase transition from a polariton Bose-Einstein condensate to a photon laser, Phys. Rev. Lett. 122, 185301 (2019).
- [11] R. Hanai and P. B. Littlewood, Critical fluctuations at a many-body exceptional point, Phys. Rev. Res. 2, 033018 (2020).
- [12] M. Fruchart, R. Hanai, P. B. Littlewood, and V. Vitelli, Non-reciprocal phase transitions, Nature 592, 363 (2021).
- [13] C. Weis, M. Fruchart, R. Hanai, K. Kawagoe, P. B. Littlewood, and V. Vitelli, Generalized exceptional points in nonlinear and stochastic dynamics, Phys. Rev. Res., (2025).
- [14] T. Barthel and Y. Zhang, Criticality and Phase Classification for Quadratic Open Quantum Many-Body Systems, Phys. Rev. Lett. 129, 120401 (2022).
- [15] T. Suchanek, K. Kroy, and S. A. Loos, Irreversible mesoscale fluctuations herald the emergence of dynamical phases, Phys. Rev. Lett. 131, 258302 (2023).
- [16] V. P. Flynn, E. Cobanera, and L. Viola, Topological zero modes and edge symmetries of metastable Markovian bosonic systems, Phys. Rev. B 108, 214312 (2023).
- [17] M. Ughrelidze, V. P. Flynn, E. Cobanera, and L. Viola, Interplay of finite- and infinite-size stability in quadratic bosonic Lindbladians, Phys. Rev. A 110, 032207 (2024).
- [18] C. P. Zelle, R. Daviet, A. Rosch, and S. Diehl, Universal phenomenology at critical exceptional points of nonequilibrium O(N) models, Phys. Rev. X 14, 021052 (2024).
- [19] Y. Avni, M. Fruchart, D. Martin, D. Seara, and V. Vitelli, Nonreciprocal ising model, Phys. Rev. Lett. 134, 117103 (2025).
- [20] K. Deng, X. Li, and B. Flebus, Exceptional points as signatures of dynamical magnetic phase transitions, Phys. Rev. B 107, L100402 (2023).
- [21] J. M. Lee, T. Kottos, and B. Shapiro, Macroscopic magnetic structures with balanced gain and loss, Phys. Rev. B 91, 094416 (2015).
- [22] P. A. McClarty and J. G. Rau, Non-Hermitian topology of spontaneous magnon decay, Phys. Rev. B 100, 100405 (2019).
- [23] D. Malz, J. Knolle, and A. Nunnenkamp, Topological magnon amplification, Nat. Commun. 10, 3937 (2019).
- [24] K. Deng and B. Flebus, Non-Hermitian skin effect in magnetic systems, Phys. Rev. B 105, L180406 (2022).
- [25] H. M. Hurst and B. Flebus, Non-Hermitian physics in magnetic systems, J. Appl. Phys. 132, https://doi.org/10.1063/5.0124841 (2022).
- [26] P. M. Gunnink, J. S. Harms, R. A. Duine, and A. Mook, Zero-Frequency Chiral Magnonic Edge States Protected by Nonequilibrium Topology, Phys. Rev. Lett. 131, 126601 (2023).
- [27] B. Flebus, S. Rezende, D. Grundler, and A. Barman, Recent advances in magnonics, J. Appl. Phys. 133, https://doi.org/10.1063/5.0153424 (2023).
- [28] H. Yuan, R. Lavrijsen, and R. A. Duine, Unidirectional magnetic coupling induced by chiral interaction and nonlocal damping, Phys. Rev. B 107, 024418 (2023).
- [29] S. Kamboj, R. A. Duine, B. Flebus, and H. M. Hurst, Oscillatory edge modes in two dimensional spin-torque oscillator arrays, Phys. Rev. B 109, 094436 (2024).

- [30] J. Zou, S. Bosco, E. Thingstad, J. Klinovaja, and D. Loss, Dissipative Spin-Wave Diode and Nonreciprocal Magnonic Amplifier, Phys. Rev. Lett. 132, 036701 (2024).
- [31] J. Slonczewski, Current-driven excitation of magnetic multilayers, J. Magn. Magn. Mater. 159, L1 (1996).
- [32] L. Berger, Effect of interfaces on Gilbert damping and ferromagnetic resonance linewidth in magnetic multilayers, J. Appl. Phys. 90, 4632 (2001).
- [33] Y. Tserkovnyak, A. Brataas, and G. E. W. Bauer, Enhanced Gilbert Damping in Thin Ferromagnetic Films, Phys. Rev. Lett. 88, 117601 (2002).
- [34] Y. Tserkovnyak, A. Brataas, and G. E. W. Bauer, Spin pumping and magnetization dynamics in metallic multilayers, Phys. Rev. B 66, 224403 (2002).
- [35] K. Di, V. L. Zhang, H. S. Lim, S. C. Ng, M. H. Kuok, J. Yu, J. Yoon, X. Qiu, and H. Yang, Direct Observation of the Dzyaloshinskii-Moriya Interaction in a Pt/Co/Ni Film, Phys. Rev. Lett. 114, 047201 (2015).
- [36] D.-S. Han, K. Lee, J.-P. Hanke, Y. Mokrousov, K.-W. Kim, W. Yoo, Y. L. Van Hees, T.-W. Kim, R. Lavrijsen, C.-Y. You, et al., Long-range chiral exchange interaction in synthetic antiferromagnets, Nat. Mater. 18, 703 (2019).
- [37] J. A. Arregi, P. Riego, A. Berger, and E. Y. Vedmedenko, Large interlayer Dzyaloshinskii-Moriya interactions across Ag-layers, Nat. Commun. 14, 6927 (2023).
- [38] X. Li, M. A. Begaowe, S. Zhang, and B. Flebus, Non-hermitian and Liouvillian skin effects in magnetic systems, Phys. Rev. B 112, 134416 (2025).
- [39] G. Tatara, Effective gauge field theory of spintronics, Physica E 106, 208 (2019).
- [40] D. Hill, V. Slastikov, and O. Tchernyshyov, Chiral magnetism: a geometric perspective, SciPost Physics 10, 078 (2021)
- [41] A. Di Pietro, P. Ansalone, V. Basso, A. Magni, and G. Durin, Gauge theory applied to magnetic lattices, Europhys. Lett. 140, 46003 (2022).
- [42] P. Ansalone, E. Olivetti, A. Magni, A. Sola, and V. Basso, Gauge theory applied to chiral magnets, AIP Advances 12, https://doi.org/10.1063/9.0000322 (2022).
- [43] É. B. Sonin, Spin currents and spin superfluidity, Adv. Phys. 59, 181 (2010).
- [44] K. Yang, K. Moon, L. Zheng, A. MacDonald, S. Girvin, D. Yoshioka, and S.-C. Zhang, Quantum ferromagnetism and phase transitions in double-layer quantum Hall systems, Phys. Rev. Lett. 72, 732 (1994).
- [45] B. Halperin and P. Hohenberg, Hydrodynamic theory of spin waves, Phys. Rev. 188, 898 (1969).
- [46] É. B. Sonin, Superflows and superfluidity, Sov. Phys. Usp. 25, 409 (1982).
- [47] C. Sun, T. Nattermann, and V. L. Pokrovsky, Unconventional superfluidity in Yttrium Iron Garnet Films, Phys. Rev. Lett. 116, 257205 (2016).
- [48] F. Wilczek, Quantum time crystals, Phys. Rev. Lett. **109**, 160401 (2012).
- [49] K. Sacha and J. Zakrzewski, Time crystals: a review, Reports on Progress in Physics 81, 016401 (2017).
- [50] X. Wu, Z. Wang, F. Yang, R. Gao, C. Liang, M. K. Tey, X. Li, T. Pohl, and L. You, Dissipative time crystal in a strongly interacting Rydberg gas, Nature Physics 20, 1389 (2024).

- [51] T. Brauner and H. Watanabe, Spontaneous breaking of spacetime symmetries and the inverse Higgs effect, Phys. Rev. D 89, 085004 (2014).
- [52] This spinor characterizes magnonic excitations which, due to bosonic statistics, transform under SU(1,1), not SU(2), like conventional Nambu-Dirac spinors. These transformations preserve the norm $|u|^2 |v|^2$.
- [53] R. Shindou, R. Matsumoto, S. Murakami, and J.-i. Ohe, Topological chiral magnonic edge mode in a magnonic crystal, Phys. Rev. B 87, 174427 (2013).
- [54] Q.-R. Xu, V. P. Flynn, A. Alase, E. Cobanera, L. Viola, and G. Ortiz, Squaring the fermion: The threefold way and the fate of zero modes, Phys. Rev. B 102, 125127 (2020).
- [55] J. H. P. Colpa, Diagonalization of the quadratic boson Hamiltonian, Physica A 93, 327 (1978).
- [56] V. Peano and H. Schulz-Baldes, Topological edge states for disordered bosonic systems, J. Math. Phys. 59, https://doi.org/10.1063/1.5002094 (2018).
- [57] V. P. Flynn, E. Cobanera, and L. Viola, Deconstructing effective non-hermitian dynamics in quadratic bosonic Hamiltonians, New J. Phys. 22, 083004 (2020).
- [58] J. Harms, H. Yuan, and R. A. Duine, Antimagnonics, AIP Adv. 14, https://doi.org/10.1063/5.0151652 (2024).
- [59] Note that, unlike for fermions, there are no true bosonic holes. A mapping $a \mapsto a^{\dagger}$ reverses the canonical commutation relations, and thus is not unitarily implementable. Nonetheless, the particle-hole language is a convenient shorthand for our BdG description.
- [60] Y. Kawaguchi and M. Ueda, Spinor bose–einstein condensates, Phys. Rep. 520, 253 (2012).
- [61] N. Hatano and D. R. Nelson, Localization Transitions in Non-Hermitian Quantum Mechanics, Phys. Rev. Lett. 77, 570 (1996).
- [62] S. Yao and Z. Wang, Edge States and Topological Invariants of Non-Hermitian Systems, Phys. Rev. Lett. 121,

- 086803 (2018).
- [63] D. S. Borgnia, A. J. Kruchkov, and R.-J. Slager, Non-Hermitian Boundary Modes and Topology, Phys. Rev. Lett. 124, 056802 (2020).
- [64] A. Metelmann and A. A. Clerk, Nonreciprocal Photon Transmission and Amplification via Reservoir Engineering, Phys. Rev. X 5, 021025 (2015).
- [65] E. Iacocca, T. J. Silva, and M. A. Hoefer, Breaking of Galilean invariance in the hydrodynamic formulation of ferromagnetic thin films, Phys. Rev. Lett. 118, 017203 (2017).
- [66] A. Roldán-Molina, A. S. Nunez, and R. Duine, Magnonic black holes, Phys. Rev. Lett. 118, 061301 (2017).
- [67] J. Harms, H. Yuan, and R. A. Duine, Enhanced magnon spin current using the bosonic Klein paradox, Phys. Rev. Appl. 18, 064026 (2022).
- [68] E. Forbes, M. D. Horner, A. Hallam, J. Barker, and J. K. Pachos, Exploring interacting chiral spin chains in terms of black hole physics, Phys. Rev. B 108, 245142 (2023).
- [69] K. Nakayama, K. Kasahara, T. Inada, and S. Tomita, Resonant amplification of spin waves with analogue black-hole horizons, Phys. Rev. Appl. 22, 064086 (2024).
- [70] M. Človečko, E. Gažo, M. Kupka, and P. Skyba, Magnonic analog of black-and white-hole horizons in superfluid ³He-B, Phys. Rev. Lett. 123, 161302 (2019).
- [71] A. Fernández-Pacheco, E. Vedmedenko, F. Ummelen, R. Mansell, D. Petit, and R. P. Cowburn, Symmetrybreaking interlayer Dzyaloshinskii–Moriya interactions in synthetic antiferromagnets, Nat. Mater. 18, 679 (2019).
- [72] C. O. Avci, C.-H. Lambert, G. Sala, and P. Gambardella, Chiral coupling between magnetic layers with orthogonal magnetization, Phys. Rev. Lett. 127, 167202 (2021).
- [73] B. Flebus, D. Grundler, B. Rana, Y. Otani, I. Barsukov, A. Barman, G. Gubbiotti, P. Landeros, J. Akerman, U. Ebels, et al., The 2024 magnonics roadmap, J. Phys.: Condens. Matter 36, 363501 (2024).